

Anisotropic fusion profile and joint strength of lotus-type porous magnesium by laser welding

Taichi Murakami^{a,1}, Takuya Tsumura^{a,*}, Teruyuki Ikeda^b,
Hideo Nakajima^b, Kazuhiro Nakata^a

^a *Joining and Welding Research Institute, Osaka University, 11-1 Mihogaoka, Ibaraki, Osaka 567-0047, Japan*

^b *The Institute of Scientific and Industrial Research, Osaka University, 8-1 Mihogaoka, Ibaraki, Osaka 567-0047, Japan*

Received 17 October 2006; accepted 24 November 2006

Abstract

The effect of pore growth direction on the weld fusion zone profile and the mechanical property of lotus-type porous magnesium joints were investigated by laser welding through experiments and numerical simulations. The dependencies of the pore growth direction on the weld fusion zone profile were evaluated on the basis of the temperature distribution calculated using the ABAQUS FE code with user subroutines. The calculated weld fusion zone profiles were in good agreement with the experimental results, thereby suggesting that thermal conductivity affects weld fusion zone profiles significantly. Moreover, the effect of pore growth direction on the joint strength of lotus-type porous magnesium was investigated. The anisotropy of the tensile strength of the lotus-type porous magnesium with regard to the pore growth direction was observed. The joints with pores parallel and perpendicular to the tensile direction were fractured at the fusion boundary and the base metal, respectively.

© 2006 Elsevier B.V. All rights reserved.

Keywords: Porous magnesium; Laser welding; Solidification; Hydrogen; Numerical simulation; Mechanical property

1. Introduction

In recent years, the development of porous metals and their applications in industries have been carried out worldwide. Such porous metals can be produced by casting, plating, powder metallurgy, and sputter deposition. The porous metals with higher porosities are called foamed or cellular-structured metals. For example, foamed aluminum with TiH₂ as the foaming agent has a unique combination of properties such as light weightness and high impact energy absorption [1,2]. However, its mechanical strength is clearly low mainly due to the stress concentration [3] because the pores are spherical and randomly distributed. On the other hand, lotus root-like (lotus-type) porous metals with pores formed by a supersaturated gas, which utilizes the difference between the gas solubilities of liquids and solids and are aligned in one direction by unidirectional solidification, possess higher strengths than the conventional porous metals

[4–7]. The strength of lotus-type porous metals, as determined by tensile tests, depends on the porosity and the pore growth direction, which is relative to the tensile direction. This can be attributed to the significant stress concentration at the pore wall when the pore growth direction is perpendicular to the tensile direction. Lotus-type porous metals are expected to serve as innovative engineering materials with various anisotropic properties, depending on the alignment of the pore growth direction.

For the industrial use of foamed and porous metals in various components, reliable joining technologies such as welding as well as processing technologies are indispensable. There have been some reports on the arc welding of cellular aluminum sandwich plates [8], laser welding and arc welding of foamable aluminum [9], arc welding of aluminum-based foam materials [10], laser welding of aluminum foams [11], diffusion bonding of closed-cell aluminum foams [12], and laser-based welding of cellular aluminum [13]. Our previous study [14] indicated that lotus-type porous copper with the pores perpendicular and parallel to the specimen surface owing to the difference in laser energy absorption on the specimen surface demonstrated significant melt anisotropy and thermal conductivity anisotropy. The difference in the laser energy absorption was considered to be the main factor because copper has a high reflectivity,

* Corresponding author. Tel.: +81 6 6879 8658; fax: +81 6 6879 8689.

E-mail address: tsumura@jwri.osaka-u.ac.jp (T. Tsumura).

¹ Present address: Institute of Multidisciplinary Research for Advanced Materials, Tohoku University, 2-1-1 Katahira, Aoba-ku, Sendai, Miyagi 980-8579, Japan.

and multiple reflections could be observed at the perpendicular pores.

Lotus-type porous magnesium, which is expected to be employed in various applications as a lightweight material, exhibits a lower reflectivity for a laser beam and lower thermal conductivity as compared to lotus-type porous copper. Therefore, it is expected that anisotropy of thermal conductivity affects the melting property of lotus-type porous magnesium much more than the difference in the laser energy absorption. From this viewpoint, the melting property is discussed in this study on the basis of comparisons between the numerical simulations and the experimental observations. Moreover, the tensile strength of lotus-type porous copper depends on the pore growth direction relative to the tensile direction because of the stress concentration at the pore wall. Therefore, a similar dependence of the tensile strength on the pore growth direction is expected for lotus-type porous magnesium. The objectives of this study are to elucidate the effect of pore growth direction on the melting and mechanical properties of welded joints with different pore growth directions.

2. Experimental procedure

Magnesium of 99.9% purity was vacuum melted in a high-pressure chamber by high-frequency induction heating. After melting, high-pressure hydrogen gas was introduced into the chamber. The pressure of hydrogen was maintained at 0.9 MPa. After hydrogen dissolved in molten magnesium at 1053 K for 1.2 ks and equilibrium was achieved, the melt was poured into the mold. The bottom plate of the mold was cooled with water circulating through a chiller. Thus, the molten magnesium was unidirectionally solidified vertically upward from the water-cooled copper-bottom plate [15,16]. The obtained ingot was 100 mm in diameter and 100 mm in height. Specimens of dimensions 40 mm × 40 mm with a thickness of 1.8 mm were cut out of

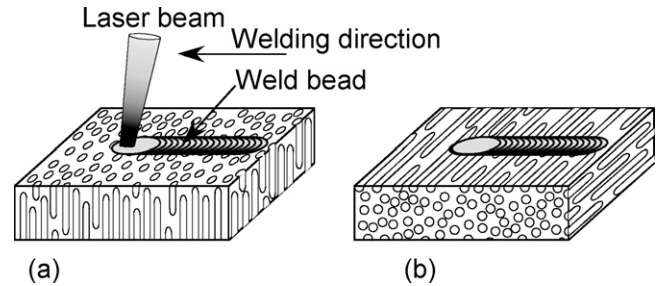


Fig. 1. Schematic views of specimens during laser welding in the porous magnesium with the pores (a) perpendicular and (b) parallel to the specimen surface.

the porous magnesium ingot with the pore growth perpendicular and parallel to the specimen surface using a spark erosion wire cutting machine (Brother Industries Ltd., HS-300). The average pore diameter and porosity of the samples were about 0.15 mm and 35%, respectively.

Fig. 1 shows schematic views of specimens during laser welding. The specimen was welded using a Nd:yttrium–aluminum–garnet (Nd:YAG) laser with a maximum nominal output power of 3.2 kW in the continuous wave mode. The wavelength of the Nd:YAG laser beam is 1064 nm, and the beam is delivered by using an optical fiber of diameter 0.3 mm. This laser beam is irradiated on the surface of the specimen at an angle of 80° to prevent damage to the optics by reflected laser beams. Argon was used as a shielding gas with a flow rate of $5.0 \times 10^{-4} \text{ m}^3 \text{ s}^{-1}$. The welding speed was maintained to be 83.3 mm s^{-1} . In this study, the process parameters selected were the laser beam power and the diameter of the laser beam at the focus point. The power of the nominal laser beam and spot diameter were varied in the range of 0.8–2.5 kW and 0.3–0.6 mm, respectively.

The cross-sections of the welded specimen were observed with an optical microscope in order to determine the profile of the fusion penetration. Fig. 2 shows the geometry of tensile

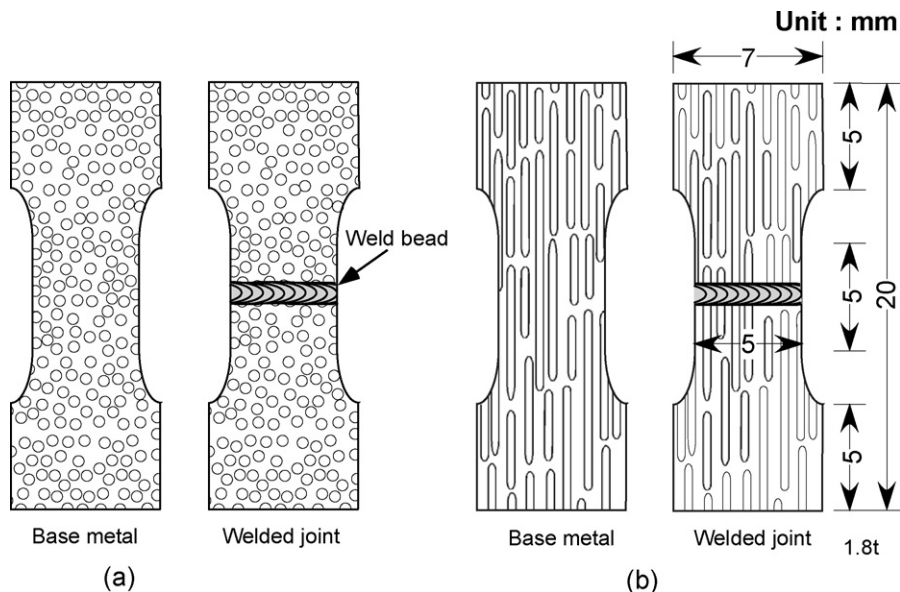


Fig. 2. Geometry in the tensile test specimens of base metal and welded joint with the pores (a) perpendicular and (b) parallel to the specimen surface.

specimens of the base metal and the welded joint. A tensile test specimen with a gage section of $1.8 \text{ mm} \times 5 \text{ mm}$ was cut out of the specimen before the welding for the base metal and after the welding for the welded joint using the spark erosion wire cutting machine. The tensile test was performed on the specimen in a tensile test machine (Toyo Baldwin, Co. Ltd., Tensilon HTM-IT) at a rate of $1.67 \times 10^{-2} \text{ mm s}^{-1}$ at room temperature.

3. Results and discussions

3.1. Characteristics of macrostructures in the welds

Fig. 3 shows the bead appearance and macrostructures in the cross-section of the welded specimen with pores perpendicular to the specimen surface at nominal laser powers of 0.8, 1.0, and 1.2 kW and spot diameters of 0.3, 0.45, and 0.6 mm. The fusion area of the specimen at the laser power of 0.8 kW and the spot diameter of 0.6 mm did not penetrate to the bottom although complete penetration of the fusion area was achieved for the spot diameter of 0.45 mm as well as for increased laser powers. This is because energy density in the former case is lower than

that in the latter case. In the weld metal, some blowholes, which form due to the remnant hydrogen gas in the original closed pores, were observed at the laser power of 1.2 kW and the spot diameter of 0.45 mm, as shown in Fig. 3.

Macrostructures of the welded joint with pores parallel to the specimen surface at different nominal laser powers are shown in Fig. 4. The weld at the laser powers of 1.5 and 2.0 kW completely melted the bottom, while the weld at the laser power of 1.0 kW did not melt the bottom completely. The blowholes, which are indicated by black arrows in Fig. 4, were observed for all the conditions. There were more blowholes in the weld metal of the specimen with pores parallel to the specimen surface (parallel case) than in the weld metal of the specimen with pores perpendicular to the specimen surface (perpendicular case). This was because the blowholes were caused by the remnant hydrogen gas in the original closed pores, and the number of original closed pores for the specimen in the parallel case was much more numerous than that for the specimen in the perpendicular case.

By comparing Fig. 3, which represents the laser power of 1.0 kW and the spot diameter of 0.6 mm, with Fig. 4(a), it was observed that the profiles of the weld metal in the perpendicular

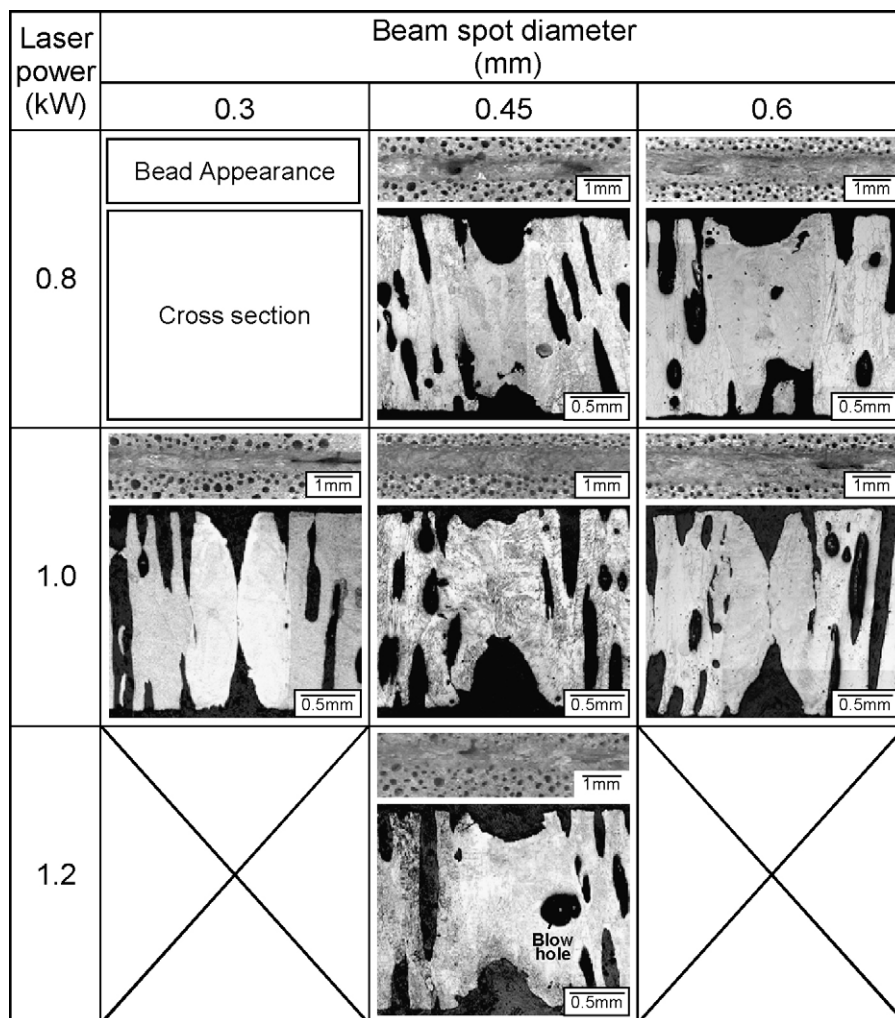


Fig. 3. Bead appearance and macrostructure of laser welded specimen with the pores perpendicular to the specimen surface at the laser powers of 0.8, 1.0 and 1.2 kW and the spot diameters of 0.3, 0.45 and 0.6 mm.

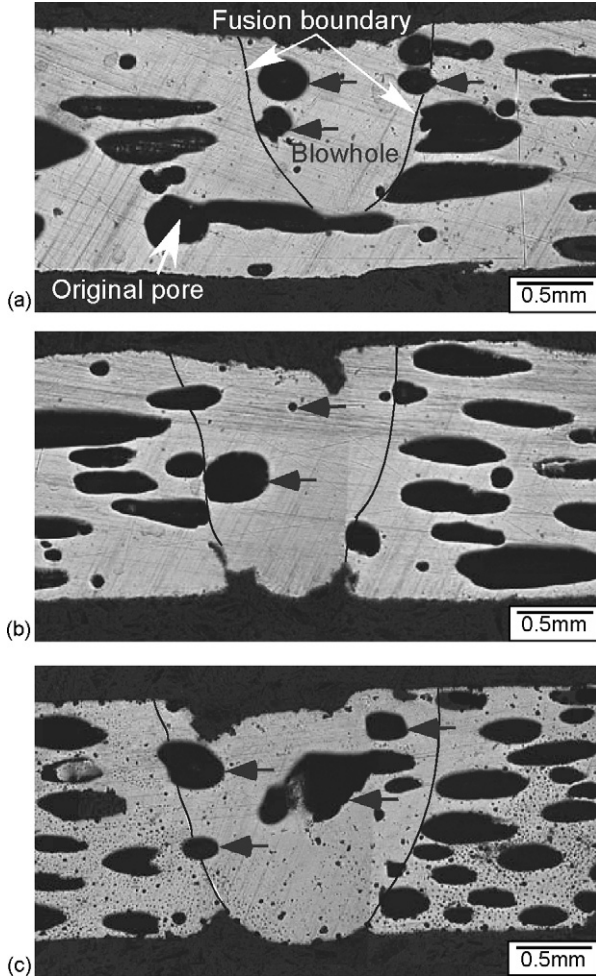


Fig. 4. Macrostructure of welded specimen with the pores parallel to the specimen surface at the spot diameter of 0.6 mm and the laser powers of (a) 1.0 kW, (b) 1.5 kW and (c) 2.0 kW.

and parallel cases were different, although the welding conditions were identical. The depth of penetration in the former case is greater than that in the latter case. In the previous report [14], the melting property of lotus-type porous copper differed greatly according to the pore growth direction. The weld bead in the parallel case was not formed in most welding conditions, and only a groove was observed. The difference in the melting property was attributed to the high reflectivity of copper for a laser beam. On the other hand, the reflectivity of magnesium is much lower than that of copper. Therefore, it is expected that the melting property of lotus-type porous magnesium is mainly controlled by the thermal conductivity. The melting property is evaluated in the next section by numerical simulations, with regard to the anisotropic thermal phenomena.

3.2. Numerical simulation of the melting property of lotus-type porous magnesium

3.2.1. Thermal modeling of lotus-type porous metal

Many reactions occur in a material during a laser welding process. A very narrow zone under the laser beam is rapidly heated, melted, and partially vaporized; then, a keyhole is formed in the

melted material. Further, the melted area of the material is solidified and it subsequently cools. In this study, thermal analysis was carried out under non-steady-state conditions in order to evaluate the melting property of lotus-type porous magnesium. Three-dimensional finite element calculations were performed, which take into account the equivalent thermal properties of lotus-type porous metals only in the first attempt along with a number of assumptions. The analyses were performed using a commercial FE code—ABAQUS.

It is assumed that a lotus-type porous metal is an equivalent homogeneous orthotropic material, in which the principal axis for the material properties is along the aligned direction of the pores. Based on this assumption, an equation for the heat conduction analysis for this type of material can be expressed as follows:

$$\rho_{\text{eq}}(T)C_{\text{peq}}(T)\frac{\partial T}{\partial t} = \frac{\partial}{\partial x} \left(\lambda_{x\text{eq}}(T)\frac{\partial T}{\partial x} \right) + \frac{\partial}{\partial y} \left(\lambda_{y\text{eq}}(T)\frac{\partial T}{\partial y} \right) + \frac{\partial}{\partial z} \left(\lambda_{z\text{eq}}(T)\frac{\partial T}{\partial z} \right) + \dot{Q}, \quad (1)$$

where $\rho_{\text{eq}}(T)$ and $C_{\text{peq}}(T)$ are the equivalent density and equivalent specific heat, respectively; x, y, z , the Cartesian coordinates; $\lambda_{i\text{eq}}(T)_{(i=x,y,z)}$, the equivalent thermal conductivity along each axis (x, y, z); and \dot{Q} is the internal heat generated per unit volume and time. The symbol (T) indicates a function of temperature T .

The thermal analysis was conducted by employing the temperature dependence of the material properties, namely, the density, specific heat, and thermal conductivity. However, there is no data on these equivalent properties for lotus-type porous metals. Therefore, the values of these properties for a lotus-type porous metal were calculated from that of a metal without pores (nonporous metal) by the rule of mixture [17]. Based on the assumption that the porosity of the lotus-type porous metal is constant with respect to the temperature change and that the equivalent density and equivalent specific heat of the lotus-type porous metals can be expressed by using the same rule as that of conventional porous metals, their equivalent properties are expressed by the following equations [18]:

$$\rho_{\text{eq}}(T) = (1 - \varepsilon)\rho_s(T) + \varepsilon\rho_f(T), \quad (2)$$

$$C_{\text{peq}}(T) = \frac{(1 - \varepsilon)\rho_s(T)C_{ps}(T) + \varepsilon\rho_f(T)C_{pf}(T)}{(1 - \varepsilon)\rho_s(T) + \varepsilon\rho_f(T)}, \quad (3)$$

where $\rho_{\text{sub}}(T)$ and $C_{\text{psub}}(T)$ are the density and specific heat, respectively, and ε is the porosity expressed by the volume ratio of pores versus the total volume of the lotus-type porous metal. The subscripts (sub) 'eq', 's', and 'f' indicate the equivalent property, property of the nonporous metal, and property of the gas in the pores, respectively. Because the density of the gas or air in the pores of the lotus-type porous metal is a thousand times smaller than that in the pores of nonporous metals, it can be neglected in Eqs. (2) and (3). Therefore, the equivalent density and the equivalent specific heat of a lotus-type porous metal are derived from the following equations:

$$\rho_{\text{eq}}(T) = (1 - \varepsilon)\rho_n(T), \quad C_{\text{peq}}(T) = C_{pn}(T), \quad (4)$$

where $\rho_n(T)$ and $C_{pn}(T)$ are the density and specific heat of the nonporous metal, respectively. Based on the assumption that the porosity dependence of the lotus-type porous metal on the thermal conductivity is the same as that of lotus-type porous copper, the equivalent thermal conductivity of the lotus-type porous metal can be calculated by using the relation between the pore growth direction and the porosity dependence of lotus-type porous copper reported by Ogushi et al. [6]. Furthermore, assuming that the porosity of the lotus-type porous metal is constant with respect to temperature change, the equivalent thermal conductivity of the lotus-type porous metal is expressed by [6]:

$$\lambda_{\text{eq}}^{\parallel}(T) = (1 - \varepsilon)\lambda_n(T), \quad \lambda_{\text{eq}}^{\perp}(T) = \frac{1 - \varepsilon}{1 + \varepsilon}\lambda_n(T), \quad (5)$$

where $\lambda_{\text{eq}}^{\parallel}(T)$ and $\lambda_{\text{eq}}^{\perp}(T)$ are the equivalent thermal conductivities parallel and perpendicular to the unidirectional pores, respectively, and $\lambda_n(T)$ is the thermal conductivity of the nonporous metal.

The temperature dependence of the density $\rho_n(T)$, specific heat $C_{pn}(T)$, and thermal conductivity $\lambda_n(T)$ of nonporous magnesium are shown in Fig. 5 and were obtained from [19,20].

3.2.2. Heat input model and boundary condition

During laser welding, a part of the irradiated laser energy is lost in the reflections at the specimen surface. The estimation of the energy loss is essential for the calculation of the temperature distribution caused by laser welding. However, it is impossible to estimate the energy loss because there is no data on the reflection from metals at high temperatures. In this study, the energy loss is assumed to be 37% of the effective laser power irradiated on the specimen surface. This value was selected because it was found to provide identical results for both the calculated penetration depth and the experimental one in the parallel case.

The heat input to the weld is generally calculated from the energy supplied to the keyhole. Many reports exist on the distributed heat source models for both arc and laser welding conditions [21–28], which were based on the Gaussian distribution of heat flux. In this study, however, the growth of the keyhole during the laser welding is modeled as follows. Fig. 6 shows the flow chart of the determination of the shape of the heat

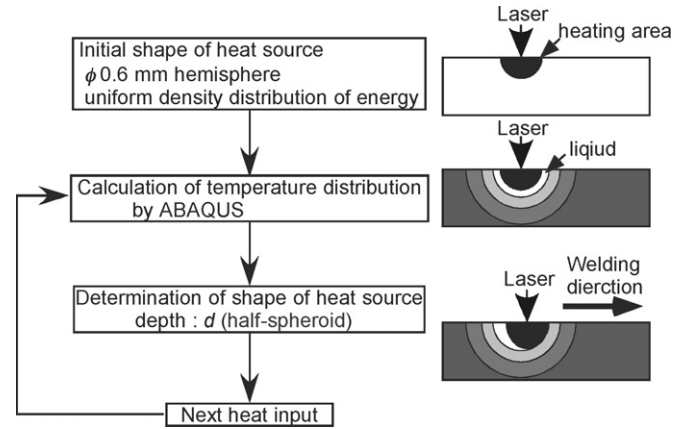


Fig. 6. Flow chart of determination of temperature distribution and shape of heat source.

source and calculation of the temperature distribution. The heat source model assumes a uniform density distribution of energy on the weld pool simulated by a half spheroid. The shape of the heat source, which changes with time, is defined as having a diameter of 0.6 mm and a depth of d mm, which is set to the depth of the weld pool at the laser spot. The location and the shape of the heat source are calculated, and the depth of the weld pool is stored by the ABAQUS user subroutine DFLUX for each time increment. Subsequently, the depth of the heat source for the next time increment is updated by the ABAQUS user subroutine UEXTERNALDB, according to the previously stored depth of the weld pool. Here, the convection in the weld metal and the heat transfer by the phase transformation are neglected in order to simplify the calculation.

The heat conduction on the specimen surface is considered only as the boundary condition. The heat loss due to the thermal radiation between the specimen and environment is neglected in order to simplify the calculation. The heat flux on the specimen surface is defined as follows:

$$q_s = \alpha_s(T_s - T_a), \quad (6)$$

where T_s is the temperature of the specimen surface; T_a , the ambient temperature; and α_s is the heat transfer coefficient. In this study, α_s is considered as $1.0 \text{ W m}^{-2} \text{ K}^{-1}$, which is the minimum value of air without flow [29].

3.2.3. Comparison between the calculated and experimental results of the weld fusion profile

Thermal analysis was carried out under the non-steady-state conditions and the temperature distribution was evaluated by the three-dimensional finite element analysis. The size of the specimen, heat input by the laser beam, welding speed, and the spot diameter were assumed to be 20 mm (x) \times 10 mm (y) \times 1.8 mm (z), 0.63 kW, 83.3 mm s^{-1} , and 0.6 mm, respectively. The initial temperature of the specimen was 298 K, and the initial depth of the heat source d was 0.3 mm. The ambient temperature T_a was assumed to be constant at 298 K. The analysis region of $y > 0$ is due to the space symmetry because the welding direction is along the x -axis. The dimension of a unit element was 0.25 mm (x) \times 0.25 mm (y) \times 0.3 mm (z). The average pore diameter and

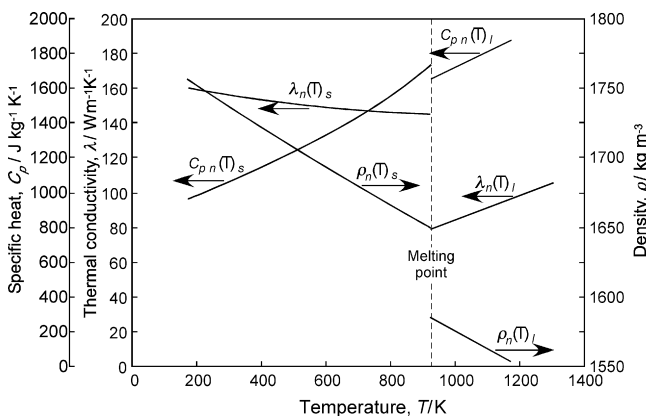


Fig. 5. Temperature dependence of the thermal conductivity, specific heat and density of nonporous magnesium [19,20].

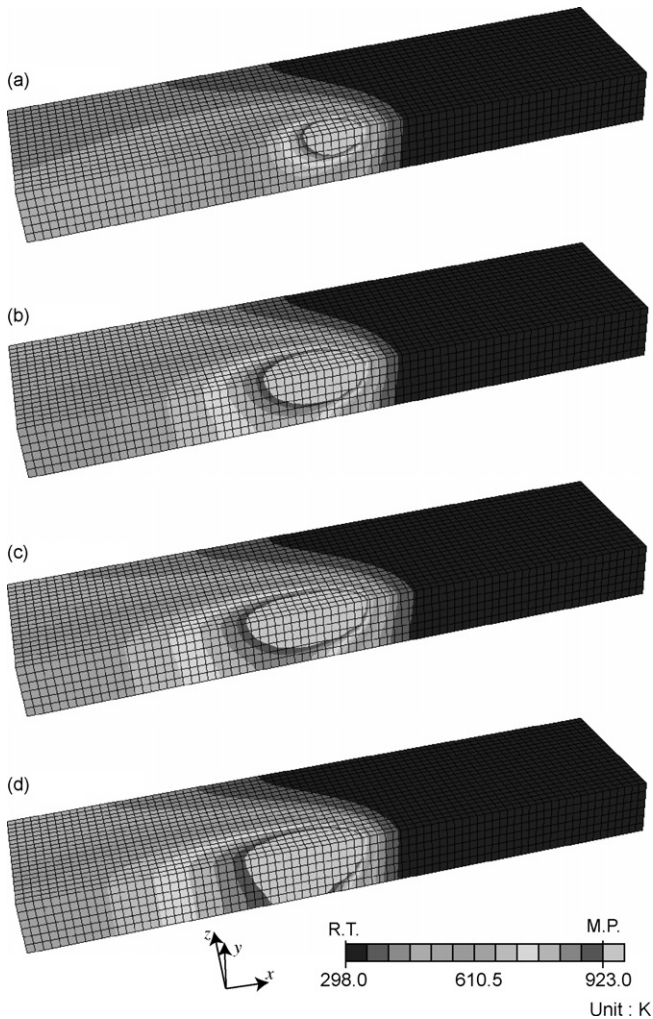


Fig. 7. Calculated temperature distribution of (a) pure (nonporous) and lotus-type porous magnesium with the pores (b) parallel to the specimen surface along with y axis, (c) parallel to the specimen surface along with x axis and (d) perpendicular to the specimen surface during laser welding process at welding time of 0.12 s. The absorbable laser power, welding speed and spot diameter are 0.63 kW, 83.3 mm s⁻¹ and 0.6 mm, respectively.

porosity of lotus-type porous magnesium in this study were 0.15 mm and 35%, respectively. From the viewpoint of the rule of mixture [17], many pores in the unit element will be required. In this study, however, the preparation of a unit element with many pores is impossible because of the limited thickness of the specimen.

Fig. 7 shows the calculated temperature distribution for specimens with different unidirectional pore directions under the same welding conditions for a welding time of 0.12 s. Fig. 7(a) shows nonporous magnesium with $\lambda_{xeq}(T) = \lambda_{yeq}(T) = \lambda_{zeq}(T) = \lambda_n(T)$; Fig. 7(b), pores parallel to the specimen surface along the y -axis (width direction) with $\lambda_{yeq}(T) = \lambda_{eq}^{\parallel}(T)$ and $\lambda_{xeq}(T) = \lambda_{zeq}(T) = \lambda_{eq}^{\perp}(T)$; Fig. 7(c), pores parallel to the specimen surface along the x -axis (welding direction) with $\lambda_{xeq}(T) = \lambda_{eq}^{\parallel}(T)$ and $\lambda_{yeq}(T) = \lambda_{zeq}(T) = \lambda_{eq}^{\perp}(T)$; and Fig. 7(d), pores perpendicular to the specimen surface with $\lambda_{zeq}(T) = \lambda_{eq}^{\parallel}(T)$ and $\lambda_{xeq}(T) = \lambda_{yeq}(T) = \lambda_{eq}^{\perp}(T)$, respectively. In Fig. 7, the regions with temperatures greater than

the melting point represent the weld pool with a keyhole. In other words, they indicate the profile of the weld metal. The size of the weld pool in the case of nonporous magnesium is smallest because its heat capacity, which is the product of the density and specific heat, is smaller than that of the lotus-type porous magnesium. Moreover, in the case of lotus-type porous magnesium, the penetration of the weld pool differs significantly in the parallel case and perpendicular case. It is considered that the difference between the weld fusion zone profiles of lotus-type porous magnesium is evaluated by the numerical simulations. The profile of the white region is mostly constant after a welding time of 0.1 s. Therefore, the profile of the weld metal was estimated using the cross-section of the maximum temperature distribution at $x = 10$ mm.

Fig. 8 shows the maximum temperature distribution in the specimen during laser welding in both the perpendicular and parallel cases along with the experimental results under the same conditions. From the calculation results, in the parallel case, the depth of the weld metal is approximately 70% of the specimen thickness. On the other hand, in the perpendicular case, the specimen melted through the bottom. These results reproduce the difference in the weld fusion zone profiles depending on the pore growth direction. However, on comparing the calculated and experimental results, it was observed that the calculated width of the weld metal was slightly greater than the experimental result. One of the reasons for this is the simplification of the analysis, in which the distributed energy density for the heat source, the convection in the weld metal, and the heat transfer by the latent heat due to the melting and vaporization of the specimen are not considered. These factors, being isotropic phenomena, do not influence the anisotropic profile of the weld metal significantly. Accordingly, the difference between the weld fusion zone profiles of lotus-type porous magnesium in both the parallel and perpendicular cases is mainly controlled by thermal conductivity anisotropy.

3.3. Tensile properties of the joints

A tensile specimen comprising a weld bead from a joint, a smooth bead, and base metals from the specimen (before welding) was obtained, as shown in Fig. 2. Subsequently, the tensile test was carried out. The tensile strengths of the weld beads and the base metals in the parallel and perpendicular cases are shown in Fig. 9 together with the cross-sectional view of the fractured joints. The open and closed circles in Fig. 9 denote the samples fractured in the base metal or in the weld bead, respectively. The average tensile strengths of the base metal in the parallel and perpendicular cases were approximately 55 and 30 MPa, respectively. The average tensile strength of the weld bead with the pores perpendicular to the specimen surface was 29 MPa, which was similar to that of the base metal because the joint was fractured in the base metal as shown in Fig. 9(b). On the other hand, the weld bead in the parallel case was fractured at the joint interface between the weld metal and the base metal as shown in Fig. 9(a). The average joint strength in the parallel case was 41 MPa, which is lower than that of the base metal for the same case.

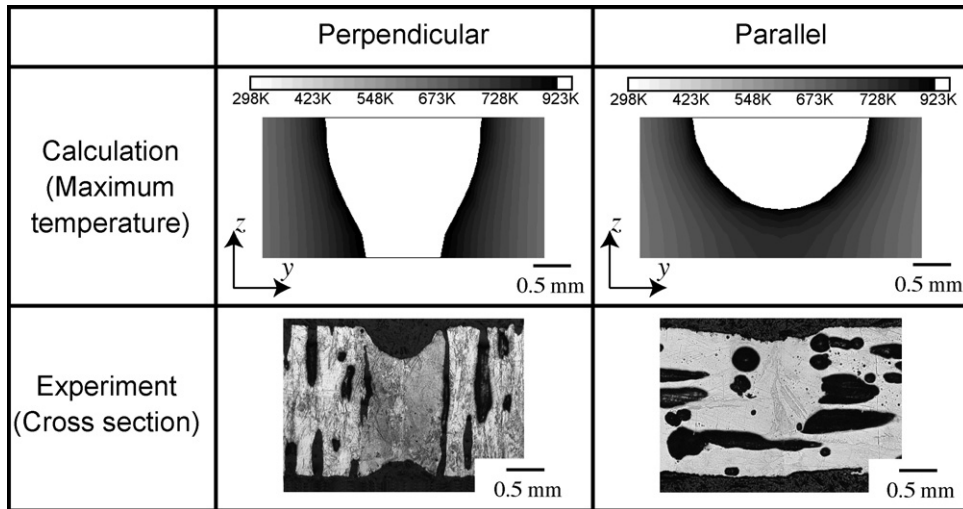


Fig. 8. Comparison between calculated maximum temperature field at the layer 10 mm in length and macrostructure of the corresponding laser weld bead with the pores perpendicular and parallel to the specimen surface.

Ikeda et al. [15,16] reported the tensile strength of non-porous magnesium produced by unidirectional solidification. The tensile strength parallel to the solidification direction was greater than that perpendicular to the solidification direction. The highly preferred orientations of the nonporous and lotus-type porous magnesium fabricated by unidirectional solidification were $\langle 0002 \rangle$ and $\langle 11\bar{2}0 \rangle$ [15,16]. The slip system of magnesium at room temperature is only $\langle 0002 \rangle \langle 11\bar{2}0 \rangle$ [30]. When a load perpendicular to the pore growth direction is applied to porous magnesium with a $\langle 11\bar{2}0 \rangle$ orientation, the $\langle 0002 \rangle \langle 11\bar{2}0 \rangle$ slip occurs because the normal direction of the $\langle 0002 \rangle$ basal plane is perpendicular to the solidification direction. On the other hand, when a load parallel to the growth direction is applied to porous magnesium with $\langle 0002 \rangle$ and $\langle 11\bar{2}0 \rangle$ orientations, the Schmid factor is close to 0. Therefore, the anisotropic tensile strength of the lotus-type porous magnesium is not only

controlled by the pore growth direction but also by the crystallographic direction.

4. Conclusions

The melting property of lotus-type porous magnesium has been studied using Nd:YAG laser welding with the laser power in the range of 0.8–2.5 kW with a welding speed of 83.3 mm s^{-1} and argon as the shielding gas, as well as numerical simulations. The results obtained are summarized as follows:

- (1) Melt anisotropy occurs when the specimen that is irradiated with a laser beam in both the perpendicular and parallel cases. In the perpendicular case, the penetration depth decreased with an increase in the spot diameter owing to the decrease in the energy density of the laser beam. In the parallel case, many more blowholes were observed as compared to the perpendicular case.
- (2) Three-dimensional finite element calculations were performed using a commercial FE code—ABAQUS. This code takes into account the thermal dependence and the difference in thermal conductivities caused by pore anisotropy. A good agreement was obtained between the calculated weld fusion zone profile and the experimental results. This indicates that the effect of the melting property on the pore growth direction against the specimen surface is controlled by the difference in the thermal conductivity caused by pore anisotropy.
- (3) Pore anisotropy of the tensile property of the joint of lotus-type porous magnesium with pores parallel and perpendicular to the tensile direction was observed because of the alignment of the pore growth direction and the crystallographic direction. For the joint with pores parallel and perpendicular to the specimen surface, the fractures were observed at the fusion boundary and the base metal, respectively.

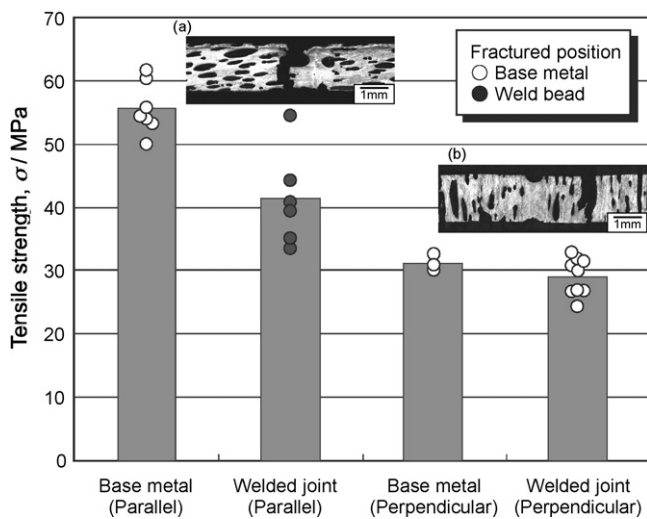


Fig. 9. Tensile strength of the base metal and welded joint with the pores perpendicular and parallel to the specimen surface together with cross-section of fractured joint. (a) Fractured in the weld bead and (b) fractured in the base metal.

References

- [1] B. Zettl, H. Mayer, S.E. Stanzl-Tschegg, *Int. J. Fatigue* 23 (2001) 565–573.
- [2] S. Ramachandra, P. Sudheer Kumar, U. Ramamurty, *Scripta Mater.* 49 (2003) 741–745.
- [3] H.P. Degischer, B. Kriszt, *Handbook of Cellular Metals: Production, Processing, Applications*, Wiley–VCH Verlag GmbH, Weinheim, 2002.
- [4] S.K. Hyun, K. Murakami, H. Nakajima, *Mater. Sci. Eng. A* 299 (2001) 241–248.
- [5] S.K. Hyun, H. Nakajima, *Mater. Sci. Eng. A* 340 (2003) 258–264.
- [6] T. Ogushi, H. Chiba, H. Nakajima, T. Ikeda, *J. Appl. Phys.* 95 (2004) 5843–5847.
- [7] S.K. Hyun, H. Nakajima, *Mater. Trans.* 43 (2002) 526–531.
- [8] U. Dilthey, M. Kessel, *Schweien und Schneiden DVS-Berichte* 220 (2002) 216–218.
- [9] Th. Bölinghaus, W. Bleck, *Cellular Metals and Metal Foaming Technology*, MIT-Verlag, 2001, pp. 495–500.
- [10] A.G. Pogibenko, V.Y. Konkevich, L.A. Arbusova, V.I. Ryazantsev, *Weld. Int.* 15 (2001) 312–316.
- [11] T. Bernard, J. Burzer, H.W. Bergmann, *J. Mater. Process. Technol.* 115 (2001) 20–24.
- [12] K. Kitazono, A. Kitajima, E. Sato, J. Matsushita, K. Kuribayashi, *Mater. Sci. Eng. A* 327 (2002) 128–132.
- [13] H. Haferkamp, J. Bunte, D. Herzog, A. Ostendorf, *Sci. Technol. Weld. Joining* 9 (2004) 65–71.
- [14] T. Murakami, K. Nakata, T. Ikeda, H. Nakajima, M. Ushio, *Mater. Sci. Eng. A* 357 (2003) 134–140.
- [15] T. Ikeda, H. Nakajima, *J. Jpn. Foundry Eng. Soc.* 74 (2002) 812–816.
- [16] T. Ikeda, H. Hoshiyama, H. Nakajima, *J. Jpn. Inst. Light Met.* 54 (2004) 388–393.
- [17] F.L. Matthews, G.A.O. Davies, D. Hitchings, C. Soutis, *Finite Element Modelling of Composite Materials and Structures*, Woodhead Publishing Ltd., Cambridge, 2000, pp. 9–10.
- [18] Japan Society of Thermophysical Properties, *Thermophysical Properties Handbook*, Yokendo Ltd., Tokyo, 1990, pp. 23, 59.
- [19] Y.S. Touloukian, R.W. Powell, C.Y. Ho, P.G. Klemens, *Thermophysical Properties of Matter; Thermal Conductivity: Metallic Elements and Alloys*, vol. 1, IFI/Plenum Data Corp., New York, 1970, 207 pp.
- [20] T. Lyman, H.E. Boyer, P.M. Unterweiser, J.E. Foster, J.P. Hontas, H. Lawton, *Metals Handbook, Properties and Selection of Metals*, vol. 1, 8th ed., American Society for Metals, Ohio, 1967, 1214 pp.
- [21] J. Mazumder, W.M. Steen, *J. Appl. Phys.* 51 (1980) 941–947.
- [22] J. Goldak, A. Chakravarti, M. Bibby, *Metall. Trans. B* 15 (1984) 299–305.
- [23] I. Miyamoto, H. Maruo, Y. Arata, *Laser Processing: Fundamentals, Applications, and Systems Engineering*, vol. 668, SPIE, 1986, pp. 11–18.
- [24] T. Zacharia, S.A. David, J.M. Vitek, T. Devroy, *Metall. Trans. A* 20 (1989) 957–967.
- [25] P. Michaleris, A. DeBiccari, *Weld. J.* 76 (1997) 172s–181s.
- [26] G. Yu, K. Masubuchi, T. Maekawa, N.M. Patrikalakis, *J. Manuf. Sci. Eng.* 123 (2001) 405–410.
- [27] W.S. Chang, S.J. Na, *J. Mater. Process. Technol.* 120 (2002) 208–214.
- [28] S.A. Tsirkas, P. Papanikos, Th. Kermanidis, *J. Mater. Process. Technol.* 134 (2003) 59–69.
- [29] Dictionary of Physics Editors Committee, *Dictionary of Physics*, reduced-size ed., Baifukan Co. Ltd., Tokyo, 1984, 1537 pp.
- [30] H. Asada, H. Yoshinaga, *J. Jpn. Inst. Met.* 23 (1959) 67–71.